Article

CO$_2$ Hydrogenation to Methane over Ni-Catalysts: The Effect of Support and Vanadia Promoting

Izabela S. Pieta [1,*], Agnieszka Lewalska-Graczyk [1], Pawel Kowalik [2], Katarzyna Antoniak-Jurak [2], Mikolaj Krysa [3], Anna Sroka-Bartnicka [3,4], Arkadiusz Gajek [1], Wojciech Lisowski [1], Dusan Mrdenovic [1], Piotr Pieta [1], Robert Nowakowski [1], Agata Lew [5] and Ewa M. Serwicka [6]

[1] Institute of Physical Chemistry Polish Academy of Science, 01-224 Warsaw, Poland; alewalska-graczyk@ichf.edu.pl (A.L.-G.); agajek@ichf.edu.pl (A.G.); wlisowski@ichf.edu.pl (W.L.); dmrdenovic@ichf.edu.pl (D.M.); ppieta@ichf.edu.pl (P.P.); rnowakowski@ichf.edu.pl (R.N.)

[2] Łukasiewicz Research Network-New Chemical Syntheses Institute, 24-110 Pulawy, Poland; pawel.kowalik@ins.lukasiewicz.gov.pl (P.K.); katarzyna.antoniak@ins.lukasiewicz.gov.pl (K.A.-J.)

[3] Department of Biopharmacy, Medical University of Lublin, Chodzki 4a, 20-093 Lublin, Poland; krysamikolaj@gmail.com (M.K.); anna.sroka@umlub.pl (A.S.-B.)

[4] Department of Genetics and Microbiology, Maria Curie-Skłodowska University, Akademicka 19, 20-033 Lublin, Poland

[5] Chemeko-System SP. z o.o, 54-519 Wroclaw, Poland; agata.lew@chemekosystem.pl

[6] Jerzy Haber Institute of Catalysis and Surface Chemistry PAS, Niezapominajek 8, 30239 Krakow, Poland; ncserwic@cyf-kr.edu.pl

* Correspondence: ipieta@ichf.edu.pl; Tel.: +48-223-432-092

Abstract: Within the Waste2Fuel project, innovative, high-performance, and cost-effective fuel production methods are developed to target the "closed carbon cycle". The catalysts supported on different metal oxides were characterized by XRD, XPS, Raman, UV-Vis, temperature-programmed techniques; then, they were tested in CO$_2$ hydrogenation at 1 bar. Moreover, the V$_2$O$_5$ promotion was studied for Ni/Al$_2$O$_3$ catalyst. The precisely designed hydrotalcite-derived catalyst and vanadia-promoted Ni-catalysts deliver exceptional conversions for the studied processes, presenting high durability and selectivity, outperforming the best-known catalysts. The equilibrium conversion was reached at temperatures around 623 K, with the primary product of reaction CH$_4$ (>97% CH$_4$ yield). Although the Ni loading in hydrotalcite-derived NiWP is lower by more than 40%, compared to reference NiR catalyst and available commercial samples, the activity increases for this sample, reaching almost equilibrium values (GHSV = 1.2×10^4 h^{-1}, 1 atm, and 293 K).

Keywords: CO$_2$ hydrogenation; methanation; Ni-catalyst; SMR catalysts; vanadium oxide catalysts

1. Introduction

CO$_2$ methanation is a process that is of great importance for power-to-gas transformation (P2G) [1–3]. Carbon dioxide captured from industrial plants, refineries, biomass combustion etc., can be converted with H$_2$ derived from water electrolysis to yield methane, synthetic natural gas (SNG). The methane production process from H$_2$ and CO/CO$_2$ was discovered by Paul Sabatier and Jean-Baptiste Senderens in 1902 and is currently considered effective for greenhouse gas removal [2]. It is also of great importance that it can be used as storage of energy coming from renewable resources (H$_2$ production by water electrolysis) in the form of gaseous fuel (CH$_4$) [4,5], allowing for filling the gap between uneven power production and power demand.

CO$_2$ hydrogenation is a highly exothermic process illustrated by Equation (1) (Table 1), where pressure and temperature significantly influence the reaction equilibrium. The process mostly focuses on C$_1$ or short-chain products CO, HCOOH, CH$_3$OH, CH$_4$, and C$_2$–C$_4$ olefins [6]. According to thermodynamics, to achieve high CO$_2$ conversion, the reaction needs to be operated at low temperature. However, low temperature implies slow

reaction kinetics and low reaction rates, especially below 523 K. On the other hand, above 723 K, the methane-yield decrease is accompanied by the CO formation as a by-product via reverse water–gas shift reaction (RWGS, Equation (4), Table 1). The high temperature also leads to the catalyst's thermal deterioration via sintering. Therefore, whether a catalyst will stay active at lower temperatures is to be determined.

Table 1. Reactions involved in CO_2 hydrogenation [1–3].

No.	Reaction	Equation		ΔH_{298K}^0 (kJ mol^{-1})
1	CO_2 methanation	$CO_2 + 4H_2 \rightleftarrows CH_4 + 2H_2O$	(1)	−165.0
2	CO methanation	$CO + 3H_2 \rightleftarrows CH_4 + H_2O$	(2)	−206.1
3	Water–gas shift (WGS)	$CO + H_2O \rightleftarrows CO_2 + H_2$	(3)	−41.2
4	Reverse water–gas shift (RWGS)	$CO_2 + H_2 \rightleftarrows CO + H_2O$	(4)	41.2
5	Methane cracking	$CH_4 \rightleftarrows C + 2H_2$	(5)	74.8
6	Boduouard reaction	$2CO \rightleftarrows CO_2 + C$	(6)	−172

Two reaction pathways are taken into consideration [1–3]. The first one consists of CO_2 to CO reduction and subsequent hydrogenation to CH_4. The second one is associated with CO_2 hydrogenation to CH_4 via the formation of carbonates and formates as intermediate species.

The implementation of a methane production technology is performed in demo-plants and industrial-scale plants [7]. ETOGAS GmbH, founded in Stuttgart by Center of Solar Energy and Hydrogen Research and later acquired by Swiss Hitachi Zosen Inova AG, is an industrial-scale plant that converts CO_2 generated in the waste-biogas plant to methane [8]. Moreover, The Karlsruhe Institute of Technology coordinates the HELMETH project, which combines high-temperature electrolysis with methanation [9]. Undoubtedly, the advantage of this process is that the heat of the exothermic methanation step can be utilized in the electrolysis process, which contributes to the efficiency increase. Electrochaea is implementing a commercial, demonstration-scale project in which bioorganisms (methanogenic archaea) are used for H_2 and CO_2 conversion to methane [10]. The microbes, patented as BioCat, are relatively resistant to contamination, have high mass conversion efficiency, and exhibit high selectivity to methane so that the generated gas can be directly used without post-treatment [3,11].

In recent years, numerous studies have been conducted on CO_2 methanation (Table S1), with the aim to develop an active, highly durable, and stable catalyst suitable for applications in the hydrogenation of CO_2 to methane [3,12]. Noble metal catalysts, such as Ru, Rh, or Pd proved to be efficient in CO_2 methanation; however, due to the high cost, their alternatives are sought for industrial applications. Ni-containing catalysts offer both high activity and affordable cost and are therefore of great interest to scientists in this field of catalysis [13]. However, for hydrogenation reaction, the Ni-based catalysts exhibit poor low-temperature activities and stabilities. Generally, for those catalysts, a temperature above 600 K is required to achieve reasonable CO_2 and CO conversions at atmospheric pressure. However, for such condition, catalyst deactivation and coke formation is reported. Thus, various promoters, supports, and preparation methods have been proposed and tested to improve catalyst activity, stability, and durability and/or move the reaction toward mild conditions (i.e., lower temperature, where Ni sintering is avoided). As previously reported, small cubic Ni nanocrystals are very selective in the methanation, while larger nickel particles are more active for the RWGS reaction. For such small nanocrystals, the hydrogenation of surface CH_x species (rds: rate-determining step of methanation reaction) by surface-dissociated hydrogen is faster than for large particles. Moreover, the carbon

formation rate was extremely slow for Ni particle sizes below 2 nm [14]. Therefore, an approach to improve the low-temperature activity while increasing coke resistance can be attained by supporting small Ni nanocrystals over suitable support, providing high Ni dispersion. Apart from forming stable anchoring sites, other crucial aspects are pore volume, acid–base properties, and structural defects, which may affect both high low-temperature activity and/or good high-temperature stability. Thus, until now, various supports for Ni catalysts have already been investigated, including Al_2O_3, SiO_2, TiO_2, and $Ce_xZr_{1-x}O_2$ [15]. In case of promoters, it was demonstrated already that a 2 wt % addition of CeO_2 increases the reducibility of Ni species and improves the stability of the catalyst in a 120 hours test [1]. In addition, highly active and coking-resistant $Ni-V_2O_3/Al_2O_3$ catalysts prepared by co-impregnation were reported with improved CO and CO_2 methanation activity [14].

Vanadium catalysts receive particular attention in the modern chemical industry. The active components of vanadium catalysts commonly used in industry include V-containing oxides, chlorides, complexes, and heteropoly salts [16]. They are used as special catalysts for sulfuric acid production, rubber synthesis, petroleum cracking, and the synthesis of some high-molecular compounds. It is well known that materials containing vanadium, with V_2O_5 as the main component, are good catalysts for the oxidation reactions [16,17]. However, only a limited amount of work has been devoted to study the role of vanadium as a promoter for low temperature CO_2 hydrogenation to methane [17]. The hypothesis is that similar to ceria, vanadia can promote the reaction by V^{3+}/V^{5+} pair. Ni- and vanadia-based catalysts are already known in many catalytic applications, i.e., steam reforming or the selective catalytic reduction of NO_x [14,18]. The Ni-V catalysts worked excellently for the biogas dry reforming (DR) as well as for methanol and dimethyl ether (DME) and steam reforming (SR) [18,19]. Moreover, the addition of vanadium oxide (V_2O_5) on the $Ni/CaO-Al_2O_3$ system was reported to improve its selectivity toward methane during CO_2 hydrogenation [20]. Thus, the catalysts are already well established, which can influence their potential application in industrial practice.

In this paper, we report the support effect on the catalytic performance, selectivity, and stability for CO_2 hydrogenation to methane under atmospheric pressure. Particular attention is placed on the reaction study in the low-temperature range where the process is kinetically limited. The vanadia influence on the catalysts' selectivity and durability in the CO_2 hydrogenation to methane is shown. The structural changes of the samples and their relevance to the sample activity are studied. Finally, we compare the difference between the preparation protocol used, impregnation, hydrothermal, and co-precipitation, and reference Ni-catalyst supported on porous alumina.

2. Materials and Methods

2.1. Synthesis, Materials, and Reagents

Ni-based catalysts, listed in Table 2, supported on different oxides, were synthesized and evaluated in this work. The metal loading in these systems is expressed in (wt %).

The Ni/Al_2O_3 and $Ni-0.5V/Al_2O_3$ (denoted as NiR and NiVR Table 2) catalysts were used as reference samples [21,22]. The NiR catalyst was prepared by a two-stage wet impregnation method with subsequent thermal treatment. The calcium-modified alumina was used as a support for the active phase ($S_{BET} = 2\ m^2g^{-1}$). Typically, the support grains were introduced into a nickel nitrate aqueous solution (220–230 gNi dm^{-3}) heated to the temperature of 306 ± 2 K and kept for 1 h. The material was separated and dried at 378 K/12 h and then was calcined at 723 K for 4 h. The whole procedure was repeated to reach an NiO content of ca. 17 wt % in the precatalyst.

To obtain an NiVR catalyst, NiR was impregnated with aqueous solutions of ammonium metavanadate (99% purity, Standard, Lublin, Poland) and oxalic acid (99% purity, POCH, Gliwice, Poland) and heated to a temperature in the range of 328 ± 5 K. The constant molar ratio of $NH_4VO_3/C_2H_2O_4 \cdot 2H_2O = 0.5$ was kept. The impregnation was sufficient to prepare the catalysts of nominal V 0.5 wt % (V_2O_5 content of 0.88 wt %). The samples were dried at 393 for 12 h and subsequently calcined at 773 for 3 h.

Table 2. Selected properties of synthesized catalysts.

Catalyst	Description	Ni Content, %	S_{BET}, $m^2 g_{cat}^{-1}$	H_2 ConsumptionT, K	D_{NiO} *, nm
Ni/α-Al$_2$O$_3$	NiR	13.4	2.0	>750	<197
Ni-V [a]/α-Al$_2$O$_3$	NiVR	13.2	2.0	603, 673,	<187
Ni/Al$_2$O$_3$	NiWP	7	223	>750	<6
Ni/SiO$_2$	Ni/Si	7	124	>750	<9
Ni/TiO$_2$	Ni/Ti	7	197	723, >750	<30
Ni/V$_x$[a]Ti$_y$O$_2$	Ni/VTi	7	179	653, 723	<50
Ni/Si$_x$Ti$_y$O$_2$	Ni/SiTi	7	137	523, 573, 723	<8
Ni/ZnO	Ni/Zn	7	18	603, 673	<36

* Obtained from DRX with Scherrer's equation of the NiO (200). [a] V content ~0.5 wt. %.

The NiWP sample was synthesized by the co-precipitation method, which is routinely employed in the synthesis of hydrotalcite-like materials [22–29]. First, Ni(NO$_3$)$_2$·6H$_2$O and Al(NO$_3$)$_3$·9H$_2$O were dissolved in deionized water (135 mL) at a molar ratio of M^{2+}/M^{3+} of 0.35, i.e., much lower than in the natural hydrotalcite (M^{2+}/M^{3+} = 3), so that the excess Al could form, after calcination, as an alumina support. Then, the metallic salt solution was added dropwise into 370 mL of 0.2 M Na$_2$CO$_3$ solution under vigorous stirring. During the synthesis process, 1 M NaOH was simultaneously added to keep pH = 10, and the temperature at 328 K was kept constant. The obtained precipitate was collected by centrifugation, washed with distilled water, and dried at 323 K in air. Finally, the dry powder was ground using an agate mortar. The mixed oxide material was obtained by calcination of the hydrotalcite-like precursor in a muffle furnace at 823 K for 4 h.

Ni/ZnO, Ni/SiO$_2$, Ni/Ti$_x$Si$_y$O$_2$, Ni/TiO$_2$, and Ni/V$_x$Ti$_y$O$_2$ catalysts were obtained via the hydrothermal method [30]. Zn (II) acetate (Zn(Ac)$_2$·2H$_2$O, 99.5% pure, Sigma Aldrich), Ni (II) acetate (Ni(Ac)$_2$·4H$_2$O, 99.5% pure, Sigma Aldrich), NaOH (>97% pure, Sigma Aldrich), C$_2$H$_5$OH (EtOH, 99.5% pure, SigmaAldrich), polyethylene glycol (PEG-400, Sigma Aldrich), tetraethylorthosilicate (TEOS, C$_8$H$_{20}$O$_4$Si, 99 % pure, Merck), titanium (IV) butoxide (Ti(C$_4$H$_9$O)$_4$, TB, 97% pure, Sigma Aldrich) and ammonium metavanadate (NH$_4$VO$_3$, 99% purity, Standard, Lublin, Poland) were used. The method was adopted from the synthesis of Ni-doped ZnO nanorods. Then, 1 mmol Zn(Ac)$_2$·2H$_2$O and the required amount of (Ni(Ac)$_2$·4H$_2$O were dissolved in absolute ethanol to form a 25.0 mL solution). Then, 8 mmol NaOH + 10.0 mL EtOH was introduced into the above solution under magnetic stirring, and 8.0 ml PEG-400 was added in one dose. The obtained slurry was transferred to a Teflon-lined stainless autoclave of 50 mL capacity and crystalized statically at 413 K for 24 h. After the reaction, the obtained precipitate was washed by absolute ethanol and Millipore water several times. The sample was dried in air at 333 K for 4 h. The final material was calcined at 773 K for 3 h. The procedure was applied to synthesize Ni/ZnO, Ni/SiO$_2$, Ni/Ti$_x$Si$_y$O$_2$, Ni/TiO$_2$, and Ni/V$_x$Ti$_y$O$_2$ catalysts.

The catalysts unloaded from the experimental reactor after activity tests (spent catalysts) were additionally labeled with "AR."

2.2. Physicochemical Characterization

The specific surface area (S_{BET}) was measured with the Micromeritics ASAP apparatus (Micromeritics ASAP 2020, USA), using the BET method and N$_2$ as the adsorbate. Before the measurement, the samples were degassed at 473 K for 3 h. S_{BET} was calculated based on N$_2$ adsorption isotherms at 77 K.

X-ray diffraction patterns (XRD) were collected using a D5000 powder diffractometer (Bruker AXS, USA) equipped with a LynxEye strip detector. Cu-Kα radiation was used with an X-ray tube operating at 40 kV and 40 mA. All measurements were performed in the Bragg–Brentano geometry. The diffraction patterns were analyzed using a multipeaks

fitting of the PseudoVoigt or Parson 7 function. Consequently, the examined diffraction reflections were deconvoluted on the identical shape $K\alpha_1$ and $K\alpha_2$ reflections with the ratio of their intensity 1:0.513. After subtracting the interpolated instrumental broadening, the FWHM of the $K\alpha_1$ reflections were used to estimate the mean diameter of crystallites using the Scherrer equation $B(2\theta) = K\lambda/D\cdot\cos\theta$, where the peak width, $B(2\theta)$, at a particular value of 2θ (θ being the diffraction angle, λ being the X-ray wavelength) is inversely proportional to the crystallite size D; the constant K is a function of the crystallite shape generally taken as being about 1.0 for spherical particles. For calculation purposes, the shape factor of 1.10665 corresponding to ball-shaped crystallites was applied.

XPS measurements were performed using a Microlab 350 instrument (Thermo Electron, USA) to determine the chemical state of the elements in the studied samples. Survey and high-resolution spectra were acquired using $AlK\alpha$ (hν = 1486.6 eV) radiation and pass energies of 100 and 40 eV. The XPS signal intensity was determined using linear or Shirley background subtraction. Peaks were fitted using an asymmetric Gaussian/Lorentzian mixed-function, and the measured binding energies were corrected based on the C1s energy at 285.0 eV.

In situ DRIFT spectra were collected in the range 700–4000 cm^{-1} on a Nicolet Nexus instrument (iS50, Thermo Fisher Scientific, USA). Typically, 100 scans were collected at a resolution of 1 cm^{-1}.

UV-vis diffuse reflectance spectra were recorded by using a Jasco V-570 instrument (Jasco, USA) equipped with a conventional integrating sphere.

The Raman data were collected using a confocal Thermo DXR Raman Microscope (Thermo Scientific, Waltham, MA, USA) with a 50× air objective. The laser wavelength used was 532 nm. The parameters were optimized to obtain the best signal-to-noise ratio. The aperture was set to 50 μm pinhole, and the laser power was 8 mW. The exposure time was 4s, and the number of exposures for one spectrum was 15. The chemical maps were made with a stepsize 1.5 μm in the x and y-axis. The whole map region was 15 × 15 μm, while the depth line maps were made with a stepsize 2 μm in the x and z-axis. The entire map area was 10 × 20 μm. The analysis of the spectra (baseline correction, deconvolution) was performed using Origin Pro Software (v. 9.1, OriginLab Corporation, Northampton, MA., USA, 2013). The deconvolution points were chosen with respect to the second derivative spectra. The chemical map analysis was achieved in the Omnic Software (v. 8.2, Thermo Fischer Scientific Inc., Waltham, MA., USA, 2010), and all maps were normalized prior to the analysis.

Temperature-programmed reduction runs (TPR, in 5% H_2 in He) were performed in a quartz tube reactor connected to a quadrupole mass spectrometer (HPR 60, Hiden, UK). Typically, 45 mg of the catalyst sample was used for each test. The sample was heated from RT to 773 K with a ramp rate of 10 K min^{-1}.

2.3. CO$_2$ Hydrogenation Tests

The CO_2 hydrogenation tests were performed under atmospheric pressure in a Catlab system (Hiden, UK), equipped with a tubular fixed-bed reactor (5 mm external diameter) and an online mass spectrometer (MS HPR 60, Hiden, UK). Usually, 40 mg of the sieved catalyst (20–40 mesh) was loaded into the reactor, and the reactor was purged with He for ca 30 min at room temperature (RT). The temperature was measured using two thermocouples to increase accuracy. Before testing, the catalysts were pre-reduced in situ upon heating from RT to 773 K at a constant rate of 10 K min^{-1} under a flow of 5% vol. H_2/He. After reaching 773 K, the temperature was maintained constant for 3 h, and then the sample was cooled to RT in He flow. A total gas flow rate of 70 ml min^{-1} was kept within all experiments (GHSV = 1.2 × 10^4 h^{-1}, at 1 atm and 293 K). Thereafter, the feed was switched to CO_2/H_2 in the molar ratio 5/1 in He balance. The pre-mixing fluxes of high-purity gases (CO_2, H_2, He) independently calibrated via Bronkhorst MFCs were used. Reaction tests were run in the temperature-programmed mode by heating up the reactor from RT to 773 K with a rate of 10 K min^{-1}. A real-time gas analyzer (MS HPR 60, Hiden, UK) was used to

analyze exhaust gas. MS was set to the MID mode, and following different m/z signals of CO, CO_2, H_2O, O_2, CH_4, and H_2 were monitored continuously by quadrupole detector, with cross-sensitivity software corrections, and eventual formation of C2+ hydrocarbons (traces if any, not discussed here). The CO_2 conversion (X_{CO2}), and selectivity for CH_4 (S_{CH4}) and CO (S_{CO}) were calculated as follows:

$$X_{CO_2} = \frac{C_{CO_2,\ in}\ \times F_{in}\ + C_{CO_2,\ out}\ \times F_{out}}{C_{CO_2,\ in}\ \times F_{in}} \times 100$$

$$S_{CH_4} = \frac{C_{CH_4,\ out}}{C_{CO_2,\ out} + C_{CH_4,\ out}} \times 100$$

$$S_{CO} = \frac{C_{CO,\ out}}{C_{CO,\ out} + C_{CH_4,\ out}} \times 100$$

where $C_{CO_2,\ in}$ and $C_{CO_2,\ out}$ are the concentrations of CO_2 in the inlet and outlet of the reactor, respectively, F_{in} and F_{out} are the total flow rates ($cm^3\ s^{-1}$) in the inlet and outlet of the reactor, and $C_{CH4,\ out}$ and $C_{CO,\ out}$ are the outlet concentrations of CH_4 and CO, respectively.

Equilibrium calculations of the methanation process at 1 bar were performed using CEA software (NASA).
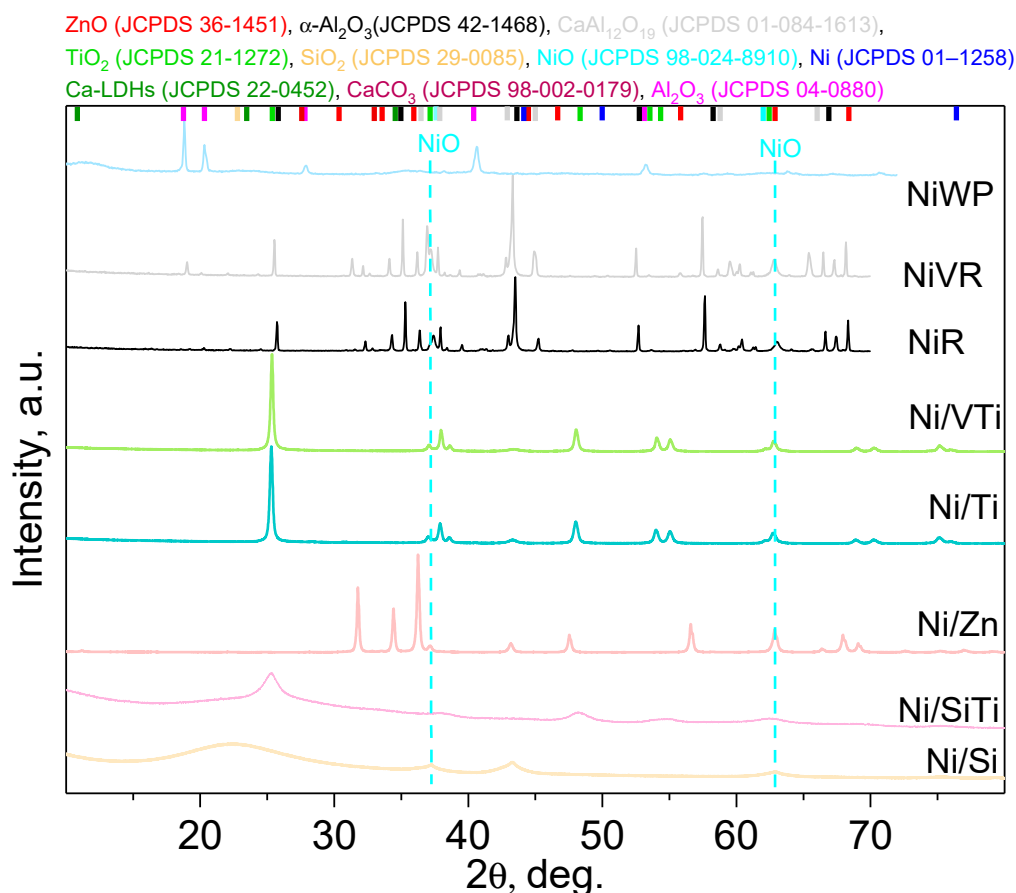
3. Results and Discussion

3.1. Physicochemical Characterization of Fresh and Spent Catalysts

The physicochemical data are summarized in Table 2. It was shown that all home-made samples have specific surface area (S_{BET}) ranging from 18.3 (Ni/Zn catalyst) to 223 m^2g^{-1} (NiWP). The NiR and NiVR samples were characterized by very low S_{BET} equal to 2 m^2g^{-1} as they contain α-Al_2O_3.

The XRD data indicated the presence of different phases for all the studied samples (Figure 1). For studied catalysts, features at 37.3° and 63° (2θ) are attributable to the NiO phase (JCPDS 98-024-8910) [31]. The hexagonal planar arrangement of Ni(II) cations with octahedral coordination of oxygen (βNi(OH)$_2$), and peaks related to vanadium species, were not detected, implying only a small quantity of these species, just below the XRD detection limit. In addition, the signals overlap with other catalysts' components in the complex XRD spectra, which was also mentioned previously [32].

For NiR and NiVR, the α-Al_2O_3 (JCPDS 42-1468) was the predominant phase, with another one associated with the presence of spinels: $NiAl_2O_4$ (JCPDS 01-078-0552) and $CaAl_{12}O_{19}$ (JCPDS 01-084-1613) [33]. For the NiWP sample, the diffractogram indicated the presence of crystalline Al_2O_3 (JCPDS 04-0880) and NiO (JCPDS 98-024-6910) phases. In addition, some broad reflections attributable to the partially reconstructed hydrotalcite-like phase, with indexing following the previously reported data (reflections at 2θ equal to 11°, 23°, and 35° JCPDS 22-0452), were evidenced [22,34,35].

The XRD pattern of the Ni/Zn nanostructured catalyst (Figure 1) shows characteristic peaks of hexagonal wurtzite structure (ZnO JCPDS 36-1451), with the strongest peaks observed at 2θ values of 31.43°, 34.5°, 36.2°, 47.2°, 56.3°, 62.4°, 67.2°, and 69.1° corresponding to the diffraction on the planes (100), (002), (101), (110), (103), (112), and (201) respectively [36]. For the Ni/Ti and NiV/Ti catalysts, TiO_2 anatase (JCPDS 21-1272) peaks are found at 2θ values of 24.6°, 37.2°, 47.6°, 53.5°, 55.1°, and 62.2°; these correspond to (101), (004), (200), (105), (211), and (204) crystal planes [33,37]. These characteristic peaks are still observed for Ni/SiTi, but they broaden. Apart from anatase, a broad peak around 22° (2θ) was attributed to amorphous silica (SiO_2 JCPDS 29-0085). This peak is also well defined in the Ni/Si sample [31].

ZnO (JCPDS 36-1451), α-Al₂O₃(JCPDS 42-1468), CaAl₁₂O₁₉ (JCPDS 01-084-1613),
TiO₂ (JCPDS 21-1272), SiO₂ (JCPDS 29-0085), NiO (JCPDS 98-024-8910), Ni (JCPDS 01–1258)
Ca-LDHs (JCPDS 22-0452), CaCO₃ (JCPDS 98-002-0179), Al₂O₃ (JCPDS 04-0880)


Figure 1. XRD patterns of the calcined samples.

In Figure 2a, the DRIFT results are presented for various Ni-supported catalysts. Three broad complex absorptions with maxima located at 700–1200, 1250–1750, and ca. 3500–3700 cm^{-1} (Figure 2a) are detected, which is in agreement with previous studies [38–45]. For the NiR and NiVR catalysts, the most intense band at ca. 1000 cm^{-1} is associated with stretching vibrations of Al–O [42]. The bands recorded below 1000 cm^{-1} correspond to the carbonate (ca. 850 cm^{-1}). The carbonate presence is expected in the prepared catalysts samples as post-synthesis residue. The shoulder at ca. 1019 cm^{-1} (Figure 2a) corresponds to the –CO_3OH modes. Moreover, these features are also typical of the spinel structure and can be related mainly to the formation of $NiAl_2O_4$ or/and $CaAl_{12}O_{19}$, as the bands at low wavenumber (usually at 700 and 570 cm^{-1}) are assigned to the so-called ν_1 and ν_2 vibrational modes of isolated tetrahedra, i.e., $[AlO_4]$ and octahedra, i.e., $[AlO_6]$, respectively [38,46].

For oxide-type material, the region of 700–1020 cm^{-1} is attributed to X-O stretching vibrations (X = Si, Ti, Zn). The features at 755 and ca 1040 cm^{-1} can suggest the Ni occupation within TiO_2, SiO_2, or mixed $Ti_xSi_{1-x}O_2$, similar to ZnO [43]. Moreover, for Ni/Zn, the band related to CO_3^{2-} was described in the region of 912 cm^{-1} and the stretching vibration of the Ni–O bond at ≈763 cm^{-1} [47]. According to the literature, this feature, assignable to an overlap of ν_4 of carbonate ion (CO_3^{2-}) together with the δOH deformation component of the hydroxide phase, is usually observed at ca. 650 cm^{-1} [38].

The 1250–1750 cm^{-1} range, most complex for NiWP and Si-containing catalysts (Ni/Si, Ni/SiTi), and V-modified samples (NiVR, Ni/VTi), is characteristic for various type of carbonates, C–O and the C=O stretching modes [38,48]. The recorded spectra exhibit the typical stretching C–O bands of carbonate at 1040–1070, 1300–1370, and 1480–1530 cm^{-1}. According to the literature, these modes are assigned as the high- and low-frequency asymmetric C–O stretching modes (ν_{3h} and ν_{3l}) and symmetric C–O stretching (ν_1), re-

spectively, which arise due to the adsorption-induced symmetry changes and the double degeneration of the ν_3 C–O stretching mode of free carbonate ion [38]. Both unidentate and bidentate carbonates were detected with characteristic features as the ν C–O bands are split into two subsets, which is indicative of the presence of at least two adsorbed carbonate species, i.e., monodentate (unidentate), weakened by co-adsorbed hydronium ion, at 1067, 1350–1365, and 1470–1486 cm^{-1}, as well as bidentate at 1040–1050 (ν_1) 1330–1300 (ν_{3l}), and 1520–1545 cm^{-1} (ν_{3h}) [49–52]. For NiWP catalyst, the appearance of carbonate bands is consistent with a partial reconstruction of the hydrotalcite-like phase confirmed by XRD.
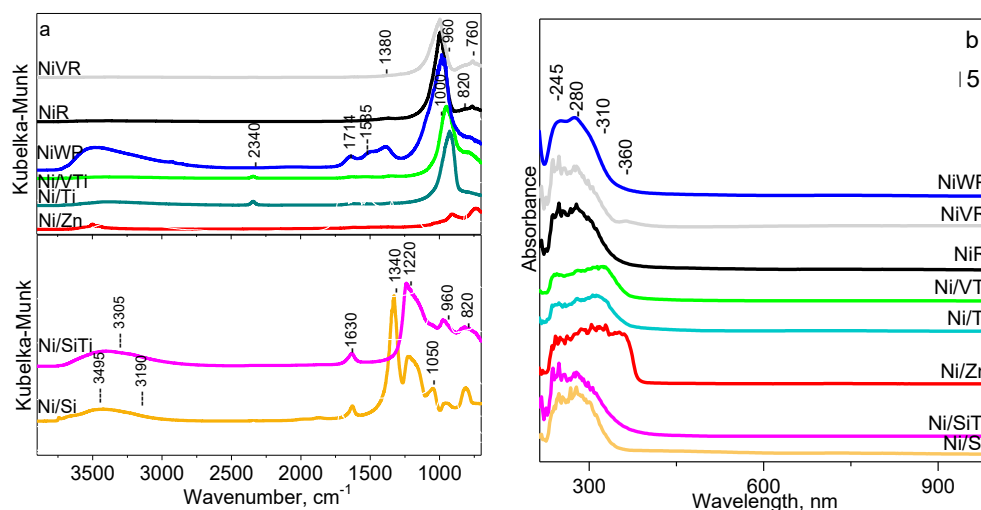
Figure 2. (**a**) DRIFT and (**b**) UV-VIS spectra of Ni-supported catalysts.

The 1350–1600 cm^{-1} range is also a fingerprint of the acetate anion, which may be a residue after the synthesis of the catalysts, as the acetate salts of Zn and/or Ni were used in the case of Ni/Si, Ni/SiTi, Ni/Ti, Ni/VTi, and Ni/Zn [52,53].

For the Si-containing samples, the DRIFT spectra of all the supports show features that are assignable to the Si–O–Si bending vibrations (830–870 cm^{-1}), the Si-OH stretching vibrations of non-bridging oxygen (950–980 cm^{-1}), the asymmetric stretching (1090–1120 cm^{-1}), the deformation vibrations of adsorbed water molecules (1600 cm^{-1}), the stretching of adsorbed water molecules (3400 cm^{-1}), and the OH vibrations of free silanol groups (3750 cm^{-1}). For the Ni/SiTi sample, the feature at 3750 cm^{-1} almost vanished along with the peak at 1340 cm^{-1}. This could be due to the addition of Ti, which led to the fixing of the free silanol groups in the Ti–O–Ti, or Ti–O–Si disordered network, impeding their vibrations [45,46,54]. In fact, for the Ni/Ti and Ni/VTi samples, the spectra closely resemble those of the alumina-supported Ni.

The broad bands at 3000–3500 cm^{-1} and 1600–1640 cm^{-1} (Figure S1a) were attributed to the OH stretching mode $\nu(OH)^-$ of physisorbed water on the catalyst surface [38,40]. For the Ni/VTi, similarly to the NiVR catalysts, V_2O_5 does not change the band position in the spectra. However, the intensity of the bands ascribed to X–O stretching vibrations (X = Si, Ti, Zn) decreases due to carbonates' presence.

The UV-Vis absorption spectra of the Ni catalysts are presented in Figure 2b, with calculated values for allowed and not allowed transitions Figure S1a. In the spectral region (200–1000 nm), molecules of the material undergo electronic transition. All the spectra are dominated by strong absorption below 400 nm, which is attributed to the intrinsic band gap absorption of the corresponding oxide types (TiO_2, SiO_2, mixed $Ti_xSi_{1-x}O_2$, and Al_2O_3) because of electron transition from the valence to the conduction band. The contributions visible in the range 200–245 nm are attributable to the $O_2 \rightarrow X^{2+}$, $O_2 \rightarrow X^{3+}$, or $O_2 \rightarrow X^{4+}$ charge transfer transition (i.e., ligand-centered transitions where $X^{2+} = Zn^{2+}$, Ni^{2+}, $X^{3+} = Al^{3+}$, $X^{4+} = Si^{4+}$, Ti^{4+}) [54]. For NiR and NiVR, the spectrum has a very sharp absorption peak at 240–300 nm due to the $O_2 \rightarrow Al^{3+}$ charge transfer transitions,

which confirms the presence of α-Al_2O_3 phase. Moreover, with these catalysts, the weak absorption of the alumina support in the region below 400 nm is likely due to trace impurities [55].

The peaks above 400 nm were assigned to metal-to-ligand charge transfer (MLCT) [56]. In all cases, Ni catalysts exhibited weak features at 590–723 nm, which can be attributed to d-d transition of Ni^{2+} [54]. The doublets at ca. 590 nm and 660 nm indicate the presence of Ni^{2+} ions in tetrahedral coordination, similarly to $NiAl_2O_4$, while the broad absorption at about 723 nm is characteristic of octahedral coordination of Ni^{2+}, typical for NiO species. It can be concluded that nickel ions are present in different environments in octahedral coordinations, which is characteristic of nickel aluminate spinel [54,57]. Thus, the performed UV-Vis study confirmed both tetrahedral ("built-in structure") and octahedral (NiO) coordination.

For Ni/SiTi, in comparison to the Ni/Si catalyst, the broadening of the peak centered at ca. 270 nm is observed, which most likely can be indicative of the presence of Ti^{4+} ions in the SiO_2 structure and/or it could be related to the higher refractive index of TiO_2 (n~2.2–2.6) particles compared to SiO_2 crystalities (n~1.45) [54,56,58–60].

For Ni/Zn, the very broad and sharp absorption edge cut off at 385 nm is observed. According to the literature, it can be attributed to the electronic transition of ZnO, but due to the strong interfacial electronic coupling between the neighboring ZnO and Ni nanoparticles, the peak broadened more than those of other investigated Ni catalysts [61,62]. The previous research related that effect to the resonant coupling between the exciton emission of ZnO and the surface plasmons of Ni nanoparticles and the close proximity of the energy level of Zn_i (-2.27 eV) in ZnO and Fermi level of Ni nanoparticles NPs (-5.05 eV), which facilitates the transfer of trapped electrons in the Zn_i defect level to the Fermi level of Ni NPs. Moreover, it can also be related to the presence of octahedrally and tetrahedrally coordinated Zn [61,62].

3.2. Catalyst Reducibility

The reducibility of the catalysts was examined by temperature-programmed reduction (TPR) over the temperature range 298–773 K. In Figure 3, the H_2 responses as a function of temperature are presented (please note that signals are multiplied for some catalysts). The TPR profiles revealed significant differences between the Ni-supported samples. It can be seen that both TPR profiles and the amount of hydrogen consumed as well as the reduction temperature are strongly influenced by the catalyst support. Moreover, the vanadia influence is also noticed for both Al_2O_3 and TiO_2-supported samples.

The TPR profile of the NiR reference catalyst shows peaks with maxima at 600, 673, and above 773 K, which can be associated with NiO bulk and small NiO crystallites (600 K), non-crystalline NiO (673 K) species, and $NiAl_2O_4$ (above 773 K) reduction, respectively [63]. This corresponds well with the literature, where the reduction of bulk NiO and non-crystalline NiO is usually ascribed to the features located at ~650 K and ~750 K, respectively, and XPS data presented in Figure 4 [64–66]. It is well known that the sample reducibility strongly depends on the metal–support interactions [3]. For Ni-based catalysts, three types of species, characterized by (i) low reduction temperature, 573–623 K; (ii) intermediate temperature, 623–773 K; and (iii) high temperature >973 K, are reported. They are attributed to the following: free NiO, which has a weak interaction with the support and is easily reduced at lower temperatures (α species); nickel species, which are not entirely associated with spinel reducible at intermediate temperatures (β type species), and nickel aluminate spinel (γ-type of Ni species), which is characterized with high reduction temperature, above 973 K [67,68]. However, the observed reduction temperature differs from those reported in literature, which can be mostly related to the standard composition of reference samples, namely metal–support interaction [69] and the presence of Ca and modifiers.
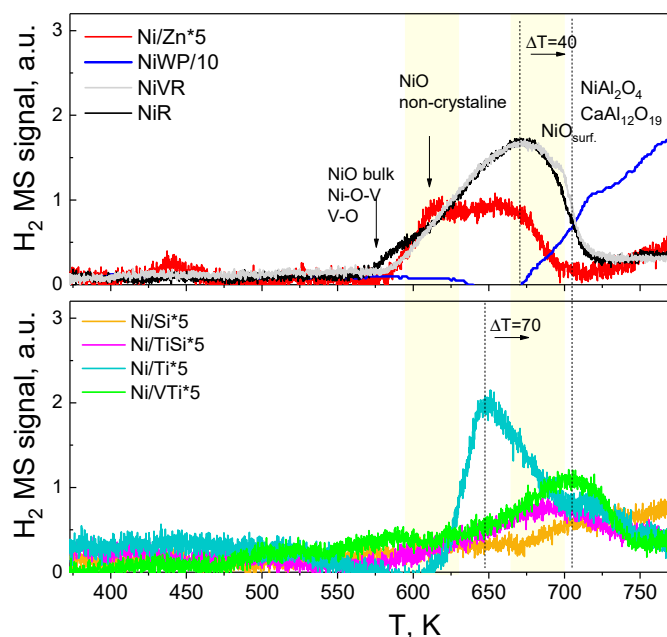
Figure 3. Temperature-programmed reduction (TPR) profiles of the catalysts (5% H_2 in He).
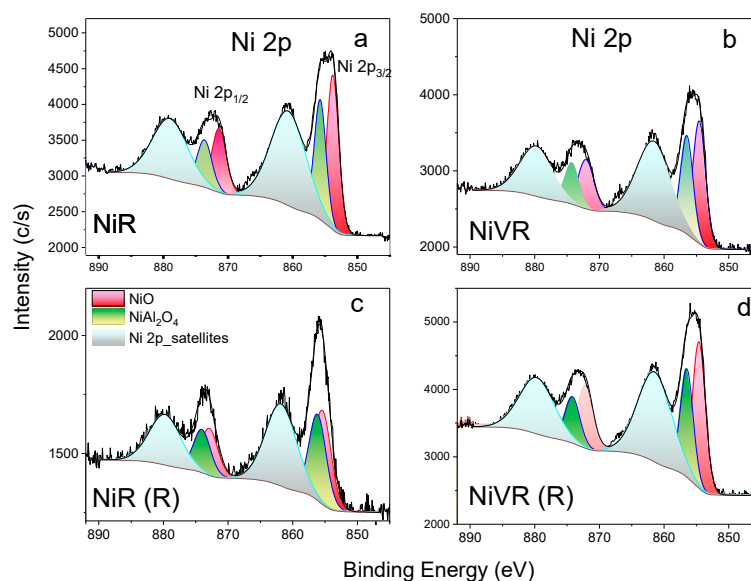

Figure 4. The HR-XPS data for Ni 2p region with deconvoluted spectra for NiR and NiVR catalysts fresh (**a**,**b**) and reduced (**c**,**d**) ((R) 5% H_2 in He).

On the other hand, NiVR shows a reduction peak shifted to a slightly higher range. It can be explained by the stronger Ni–support interactions caused by vanadia doping [66], as shown by an XPS study (Figure 4).

The amphoteric properties of V_2O_5 influenced the number of exposed Ni species, and therefore, the number of reducible NiO species increased [70]. In both catalytic systems, Al_2O_3- and TiO_2-supported hydrogen consumption starts at 500 K for NiV/Ti and 550 K for NiVR, while the hydrogen consumption maxima are shifted toward a higher region by 70 and 10 K, respectively. On the other hand, it is also expected that together with the Ni-species, the V_2O_5 undergoes simultaneous reduction, thus increasing the H_2 uptake. Usually, one single reduction peak during the TPR is observed for vanadium oxide catalysts if up to four layers of vanadium oxide are deposited on TiO_2 [71]. Similarly, for the V_2O_5/Al_2O_3 catalyst, the reduction onset at 600 K, and the peak maximum located at

800 K were reported and referred to V^{5+} to V^{3+} reduction [72]. Therefore, the reduction shift for the V-containing samples can be related to the presence of the vanadia phase and most likely attributable to the reduction of the vanadia phase, as stated above.

For NiWP, prepared by precursor co-precipitation and subsequent calcination at 823 K, a very broad signal of hydrogen consumption is visible. The hydrogen consumption started from ca. 675 K, with the maximum outside the recorded temperature range (>773 K). Among other catalysts, Ni/Zn exhibits an H_2 uptake maxima at 615 and 650 K, suggesting NiO–support interactions of weak and medium strength, respectively. For Ni/Si, no change in hydrogen signals is observed in the investigated temperature range.

The Ni 2p core-level XPS spectra (Figure 4) show the doublet Ni 2p3/2 and Ni2p1/2 and their shake-up satellites. Two different types of Ni species can be distinguished for the investigated catalyst, as indicated by the splitting of the peak at 854–856 eV. For fresh catalysts, the signals at 854.6–855.4 eV are related to Ni^{2+} (NiO) and at 856.1–856.4 eV to Ni^{2+}, strongly interacting with alumina or in the form of the spinel $NiAl_2O_4$. For fresh catalyst samples (Figure 4a,b), the most intense peak is associated with Ni^{2+} as NiO, indicating that those species are present on the catalyst surfaces in higher proportion compared to spinel-type species [20]. For the reduced NiR sample, the signal intensity related to NiO oxidic to spinel species equals almost unity, while for NiVR, the most intense peak is associated with Ni^{2+} as NiO, revealing that NiO species are present on the catalysts' surfaces in a higher proportion compared to spinel-type species (Figure S2). This could indicate that the V incorporation prevents the formation of a hardly reducible spinel. However, it is hard to conclude the alloying of those two metals, as the vanadia signal is largely shielded by O1s.

3.3. Catalyst Activity

The activity results of the catalyst in a methanation reaction are shown in Figure 5. The mass spectra (MS) profiles of the reactor outlet gases are presented along with the equilibrium calculated data. Before the reaction, the catalyst samples have been activated by an in situ NiO to Ni reduction in a H_2 stream.
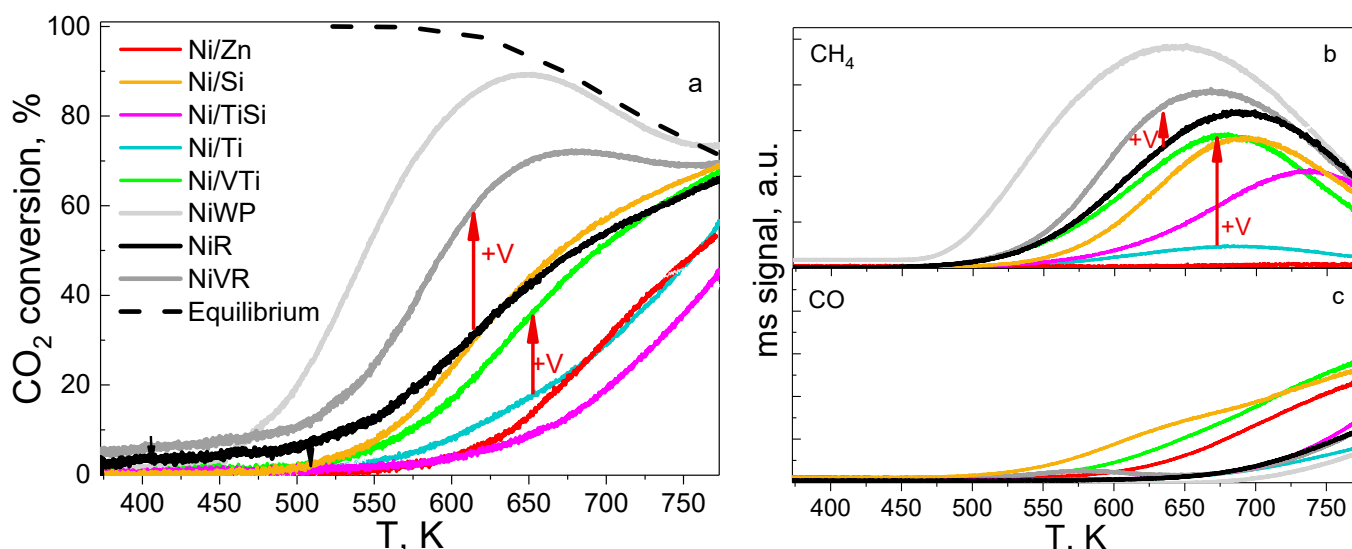
Figure 5. CO_2 conversion (**a**), CH_4 selectivity (**b**), and CO selectivity (**c**), as a function of temperature and for Ni-supported catalyst (NiWP and reference NiR, NiVR) performance given for comparison). Reaction condition GHSV = 1.2×104 h^{-1}, 1 atm and 293 K) CO_2/H_2 in the molar ratio 1/5.

The data for C-species, namely CO_2, CH_4, and CO, as well as for H_2O, were continuously monitored. Catalysts can be divided into two groups regarding their activity in carbon dioxide methanation: alumina-supported catalysts—NiWP, NiR, and NiVR and

catalysts deposited on other supports, Ni/Zn, Ni/Si, Ni/TiSi, Ni/Ti, and Ni/VTi. The former group shows significantly better performance (considering CO_2 conversion and CH_4 yield) than the latter. Moreover, the obtained Ni-based vanadia promoted catalysts outperform the reference NiR, while NiWP shows high activity, much higher than reported in the literature, as shown in Table S1. It is worth emphasizing that although the Ni loading in NiWP is lower by more than 40%, compared to the reference NiR, the activity increases for this sample, reaching almost equilibrium values. Moreover, it has a far higher S_{BET} than NiR and NiVR. For the studied process, the reaction described by Equations (1)–(3) in Table 1 are considered; however, reactions 1 and 3 are of higher importance due to enthalpy values.

For NiWP, NiR, and NiVR, the CO_2 conversion begins between 400 and 450 K. In contrast, for other catalysts, it is shifted to higher temperatures—above 500 K. However, for this region (below 573 K), the conversion of CO_2 is kinetically limited, as the conversion profiles are remarkably below the thermodynamic equilibrium curve (Figure 5a). For the NiWP and NiR catalysts, the CO_2 conversion and CH_4 yield maxima are observed between 630 and 670 K, and they almost match the values allowed by thermodynamics. The corresponding CO profiles showed that the RGWS is negligible for those catalysts. For other-oxide-supported catalysts, CO_2 equilibrium conversion is approached at the higher temperature range i.e., above 750 K. In the case of the CH_4 signal, the maxima are present between 670 and 740 K for NiVR, Ni/Zn, Ni/Si, Ni/TiSi, Ni/Ti, and Ni/VTi [73,74]. As previously reported, small cubic nickel nanocrystals are very selective in the methanation, while larger nickel particles are more active in the RWGS reaction [75]. This is valid for specific support, possibly possessing weak basicity. In the case SiTi support, although small NiO crystallites were obtained, the activity toward methanation is poor.

The catalyst activity has been compared at 600 K and displayed in Figure 6.
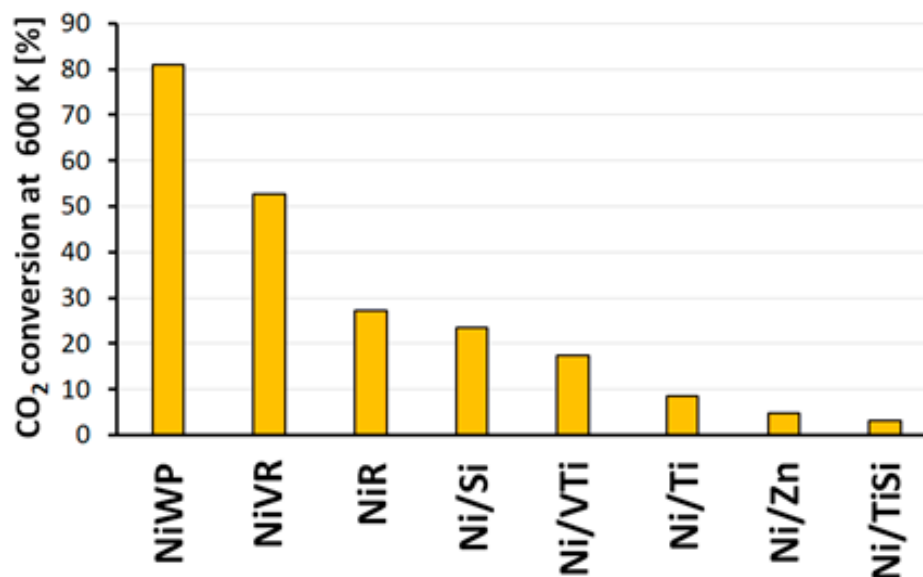

Figure 6. Catalyst activity measured as CO_2 conversion at 600 K.

Relatively high activity of alumina-based catalysts (NiWP, NiR, and NiVR) may be associated with the basicity of the support and its capacity to adsorb CO_2. Research-based on temperature programmed desorption of CO_2 (CO_2-TPD) conducted by Pandey and Deo revealed that the amount of CO_2 adsorbed on the support follows the trend Al_2O_3 > TiO_2 > ZrO_2 > SiO_2 and is the highest for alumina [76]. Moreover, due to the strong metal–support interactions in Al_2O_3, NiO crystallites are better dispersed and well-stabilized, avoiding sintering and Oswald ripening [77]. On the other hand, it is visible that catalysts based on titania (Ni/Ti, Ni/TiSi) have the lowest activity in CO_2 methanation among the investigated samples.

While comparing vanadia-doped Ni/VTi with pristine Ni/Ti, it is visible that the addition of vanadia significantly enhances the catalyst's activity, which is reflected by higher CO_2 conversion and CH_4 yield and initiation of the reaction at a lower temperature (500 K vs. 550 K, respectively). Such an effect of vanadia as a promoter has already been reported [70,78]. Hamid et al. showed that promotion with vanadia increases the basicity of the catalyst, providing additional CO_2 adsorption sites leading to the formation of unidentate carbonates [70]. Those kinds of species are considered the most reactive form, thus facilitating the hydrogenation reaction. This was proved by calculating the activation energy, which was lower for vanadia-doped than a bare nickel catalyst. The authors also showed that the V_2O_5-doped fibrous silica-based Ni/KCC-1 catalyst exhibited better NiO dispersion. During the H_2-TPR measurement, enhanced ß-stage reduction of NiO was observed, and the signal was shifted to higher temperatures, pointing to a higher exposure of Ni species for the methanation reaction and stronger Ni–support interactions providing their better stabilization [70]. Lu et al. also described the positive effect of vanadia doping on the Ni catalyst deposited on modified bentonite, where the higher NiO dispersion, better separation of catalyst particles, and smaller crystallite size, along with stronger NiO–support interactions, were confirmed by XRD and TPR measurements [78]. Moreover, the performed investigation by XPS revealed an electronic effect of VO_x species, which increased the electron cloud density of Ni atoms [78]. Examination of the reduced and used catalyst points to the occurrence of redox cycle between V^{3+}, V^{4+}, and V^{5+} in the methanation reaction. Nevertheless, vanadia's addition has a positive effect on CO_2 conversion and methane yield only to some extent. The dopant excess can lead to covering the catalytically active sites and activity loss [70,78].

It is well known that CO can be produced during the CO_2 methanation process, which is mainly due to the reverse water–gas shift reaction (RWGS) (Table 1, Equation (4)) [18,41]. Temperature rise leads to a decrease in CH_4 production along with the increase in the CO formation [79–81]. For Ni/Si, Ni/VTi, and Ni/Zn, the CO production is initiated between 500 and 550 K and keeps increasing with a rising temperature. The shape of the CO curve is unique for NiR, as it ascends at 530 K, reaches a maximum at 570 K, and descends to get the initial level at 630 K, followed by the next increase from 650 K until the end of the temperature range. For the rest of the catalysts, CO production is observed above 600 K. Therefore, it can be stated that alumina-containing catalysts are the most selective to methane in the examined temperature range. Interestingly, vanadia in Ni/VTi enhances not only CH_4 yield but also CO yield compared to Ni/Ti. Moreover, the RWGS reaction is initiated in a significantly lower temperature in the presence of vanadia.

Previous research has shown that a ceria-promoted catalyst leads to the efficient activation of CO_2, because of oxygen vacancies in ceria caused by the existence of Ce^{3+}/Ce^{4+} ion pairs [82]. A similar effect can be observed for NiVR and NiV/Ti catalysts, i.e., similar to ceria, surface methanation is enhanced by V^{3+}/V^{5+} pair. In addition, V_2O_5 presence influences the catalyst structure changes, as shown by the detailed study of the catalysts' physicochemical properties. Thus, the enhanced activity can be attributed to (i) the V-Ni interaction (alloying V and Ni and a cubic solid solution formation, which was shown to be much more active than Ni) [83]; (ii) the amphoteric properties of V_2O_5, which can provide additional adsorption sites of CO_2 [70]; and (iii) the increase in the number of accessible NiO species [78] overall, leading to lower light-off temperatures.

3.4. Catalyst Stability

The stability of best-performing catalysts with different Ni loading (13% NiR and NiVR vs. 7% NiWP) was studied for 72 h-on-stream at 623 K. Almost 90% conversion with 100% selectivity to methane was observed for NiWP catalyst in the whole time studied, as shown in Figure 7.
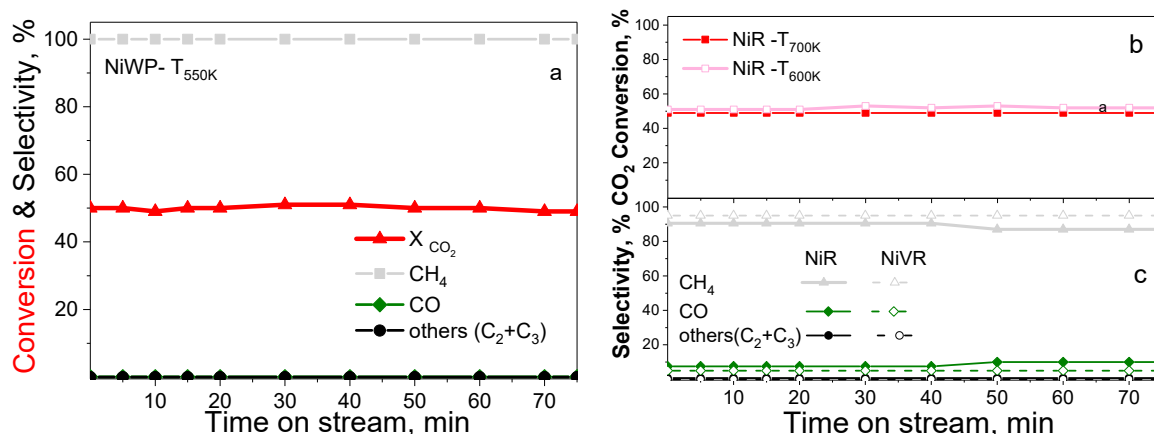
Figure 7. Stability test and selectivity to CH_4, CO, and other C_2–C_3 products at 50% CO_2 conversion in the function of time-on-stream up to 72 h for (**a**) NiWP, (**b,c**) NiR, and NiVR catalysts (temperature, where 50% CO_2 conversion was attained for each catalyst, is displayed in the panels).

In contrast, NiR catalysts exhibit a CO_2 conversion hardly reaching 50%, with selectivity toward CH_4 slightly decreasing from 98.0% to ca. 97.0% (Figure 7). The addition of vanadia improved both CO_2 conversion and selectivity to methane, obtaining values near 100%. The catalysts were characterized after the 72 h on-stream reaction. Temperature-programmed oxidation runs, under $5\%O_2$/He flow, showed no relevant carbon-related signals while increasing temperature up to 773 K, indicating limited coking occurring upon H_2-reach streams, if any (Figure 8). Moreover, the high resolution transmission electron microscopy (HRTEM) study shows only small changes in NiO average crystallites size (less than 15%) [20]. Thus, the slight crystallites sintering in the case of NiVR sample is most likely compensated by the presence of the amphoteric V_2O_5, which influences the number of exposed Ni species. Moreover, vanadia will act as an oxidation catalyst, preventing catalyst coking [20].

The slight changes in the support have been detected upon stability test as presented in Figure 8 for NiR and the NiVR vanadia-modified sample (Figures S3–S7 for other studied oxide supported catalysts). The average Raman spectra collected before and after reaction (AR) for NiR and NiVR are presented in Figure 8a–d, respectively, with corresponding maps given in Figure 4e.

The NiR spectrum before reaction (Figure 8a) shows two bands attributable to isolated octahedral AlO_6, at 421 cm^{-1} and 517 cm^{-1}, and one of significantly lower intensity at 763 cm^{-1} assigned to isolated tetrahedral AlO_4 [84,85]. The corresponding chemical maps of the NiR before reaction (Figure 4e) show that all of the bands related to alumina octa- and tetrahedra (AlO_x) are distributed evenly throughout the whole sample. Similarly, for NiR after reaction (Figure 4a vs. Figure 4b), bands at 407 cm^{-1} and 575 cm^{-1} and one band at 689 cm^{-1} attributable to isolated AlO_6 and AlO_4 are present [84,85]; however, they have significantly lower intensity. Moreover, they are red shifted, thus indicating a slight change of the support (Ca-modified porous Al_2O_3) during the reaction. In addition, in NiR AR, the bands at 1347 cm^{-1} and 1580 cm^{-1}, characteristic of disordered graphite (D band) and highly crystalline graphite (G band), respectively, were detected [86]. Usually, they are used to calculate the coke's disorder in spent catalysts and the size of the graphite microcrystals in the sample, as the ratio ID/IG relates to the average graphite domain dimension [87]. Those bands were observed only for spent alumina-supported catalysts, as shown in Figure 8 and Figures S2–S6. The relative intensity of the ID/IG bands is higher than unity, indicating that the coke crystallite size is bigger than 30 Å.

The corresponding chemical maps for NiR AR (Figure 8e) revealed that the bands distribution corresponding to AlO_x does not correlate with the D and G bands' distribution. Moreover, the regions of the D band's low intensity are similar to the regions of low intensity of the G band. In pure graphite, the G peak is narrow, and the broadness of the peaks can be

related to the degree of disorder/inhomogeneity in the deposited coke on the catalyst. Both of these features have very high intensity, with no correlation with AlO_x-related bands, thus indicating that the methanation reaction was robustly catalyzed by Ni-species leaving a carbon deposit via methane cracking or Boduouard reaction (Equations (5) and (6); see Table 1).
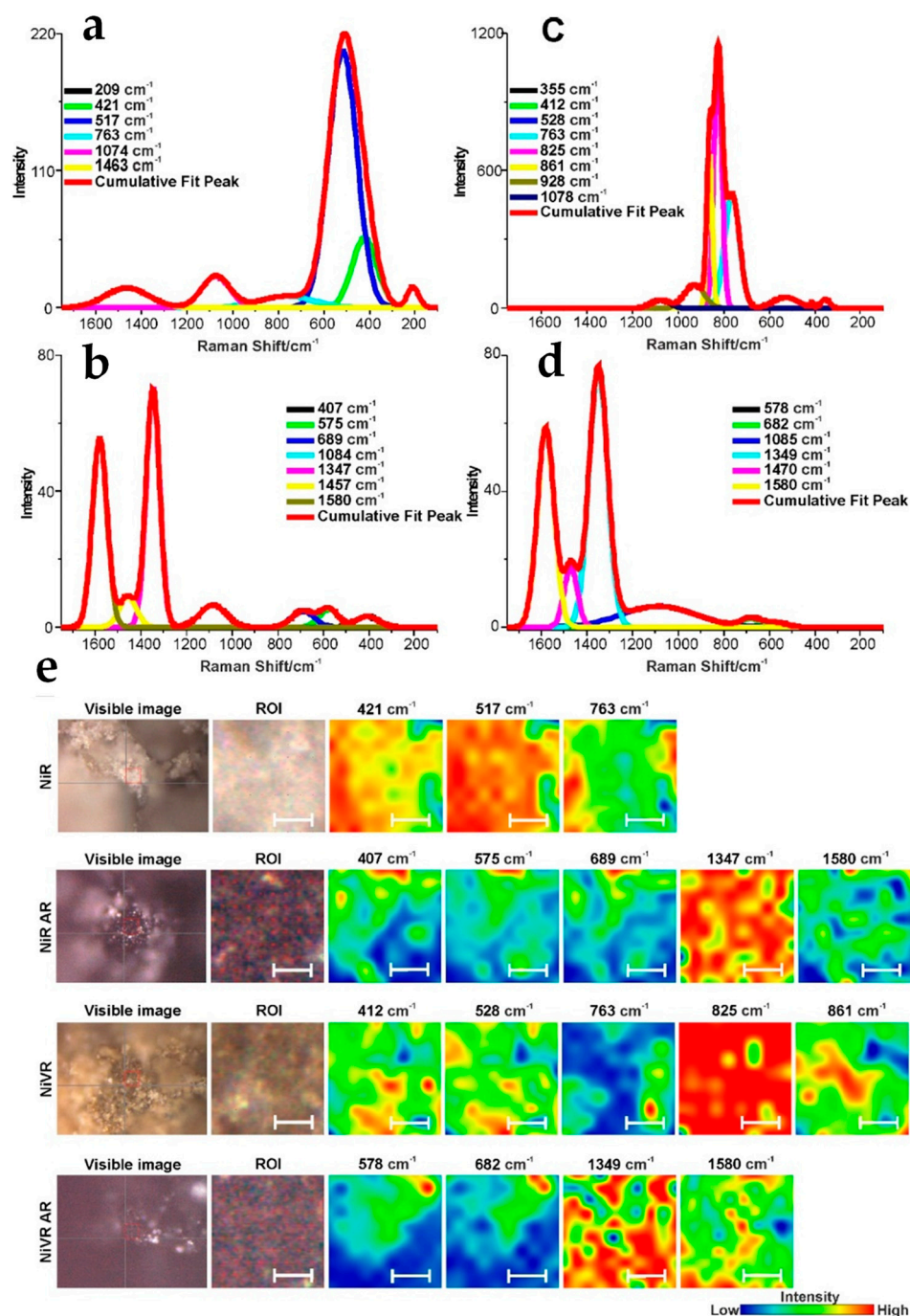
Figure 8. Raman deconvoluted spectra and chemical maps of NiR and NiVR samples before and after reaction (AR). (**a**) NiR before reaction spectrum, (**b**) NiR AR spectrum, (**c**) NiVR before reaction spectrum, (**d**) NiVR AR spectrum, (**e**) Raman maps with the distribution of selected bands for NiR before reaction, NiR AR, NiVR before reaction, and NiVR AR. Red spectra correspond to the cumulative spectrum consisting of the deconvoluted bands, other colors of the spectra correspond to the single deconvoluted bands. The white scale bar corresponds to 4.5 μm.

The analysis of the confocal depth map showed a similar distribution of the band intensities in the samples before and after the reaction—the bands on the surface were the most intense, while the deeper bands were less intense in both samples. When the intensity of the AlO_x-related bands with the confocal depth profiling of the NiR AR sample is analyzed, it can be noticed that the bands' intensity changes with the sample depth.

This fact could be related to the sample transparency and technical resolution of the spectrometer; on the other hand, it may suggest surface changes evoked by the diffusion and segregation of abundant surface elements.

The average Raman spectra of the NiVR before and after the reaction are presented in Figure 8c,d, respectively. The spectrum of NiVR before reaction shows bands at 412 cm^{-1}, 528 cm^{-1}, and 763 cm^{-1}, ascribed to isolated octahedral AlO_6, and isolated tetrahedral AlO_4, respectively. However, in contrast to the V-free sample (NiR), the bands corresponding to isolated octahedral AlO_6 have significantly lower intensity than the bands related to tetrahedral AlO_4, thus implying that vanadia changes the catalyst structure. Presumably, this can indicate the V–Ni interaction, as stated previously for Ni–V systems where a cubic solid solution formation (Ni and V alloys) was shown and explained [83].

In the NiVR sample, after the reaction (Figure 8d), the bands at 578 cm^{-1} and 682 cm^{-1} were attributed to AlO_6 and AlO_4 [84,85]. The significant shifts (ca. 60–100 cm^{-1} for condensed octahedral and isolated tetrahedral) along with the lack of some of the bands can be attributed to changes in the catalyst structure during the reaction. While for NiVR, the bands corresponding to AlO_6 reversely correlate with the band assigned to the isolated, the condensed tetrahedral structures are independent of other aluminum structures. They occur in the highest amounts in the NiVR sample before the reaction (Figure 4e). In the AR sample, there is a reverse correlation between the aluminum bands and the bands corresponding to graphene and imperfect graphite (NiVR vs. NiVR AR). Therefore, it can be concluded that the catalysis structural changes have been limited after the vanadia modification. This was also evidenced by the analysis of the confocal depth map, which showed a similar distribution of the band intensities in the samples before and after the reaction—the bands on the surface were the most intense. In contrast, the deeper bands were less intense in both of the samples. The bands corresponding to AlO_x were less intense in the depth of the sample after the reaction.

4. Conclusions

The CO_2 hydrogenation to methane technology has been known for many years as a method of carbon dioxide conversion to chemical raw materials and fuels, including drop-in-fuels. Similar to the CO_2-to-methanol process, it is considered a relatively mature concept. Nevertheless, the crucial issue for increasing the efficiency of the process is finding a durable catalyst showing high activity in a low-temperature range.

The obtained results over the Ni-based catalyst supported on various oxides revealed an excellent performance of NiWP catalysts derived from a hydrotalcite-like precursor. Although the Ni content (7 wt %) in NiWP sample is low, the catalyst outperforms the reference NiR and NiVR catalysts, supported on porous alumina. However, this catalyst was prepared by applying the co-precipitation method, which led to (i) an increase in the specific surface of the sample, (ii) the formation of the small Ni nanocrystallites with an average diameter size of ca. 6 nm. It resulted in improved catalytic activity at low-temperature CO_2 methanation.

All catalysts showed activity toward a CO_2 hydrogenation reaction. The CO_2 conversion at temperatures around 623 K almost matches the values allowed by thermodynamics for the NiWP catalyst, while for reference, the NiR and the NiVR catalyst were 43% and 67%, respectively. Among other materials at 623 K, only Ni/Si shows similar conversion to that obtained for NiR. For other oxide-supported catalysts, the CO_2 conversion increased with temperature and approached maxima above 700 K, revealing the influence of the support on the sample activity and selectivity. The primary reaction product was CH_4, while CO was detected for catalysts with increased surface acidity. Moreover, an evident

vanadia promotion is observed for both NiVR and NiV/Ti systems. Vanadia incorporation changes the catalyst's structure as a result of which the activity of the V-modified catalyst increases. The investigation results lead to the conclusion that vanadia promotion of a Ni/Al$_2$O$_3$ creates low-temperature activity toward CO$_2$ methanation and provides the opportunity to design modern catalysts, which may be attractive in the hydrogen economy and the CO$_2$ utilization industry

Supplementary Materials: The following are available online at https://www.mdpi.com/article/10.3390/catal11040433/s1, Figure S1: DRIFT spectra of Ni-supported catalysts, (a) whole range spectra (b) enhanced OH- region. UV-VIS spectra (a,b) and Tauc plots for allowed (c) and not allowed transitions (d) for Ni-supported catalysts, Figure S2. Raman spectra and chemical maps of the NiSiO$_2$ before and after reaction (AR), Figure S3. Raman spectra and chemical maps of NiTiO$_2$ before and after reaction (AR). The Figure S4. Raman spectra and chemical maps of the NiVTiO$_2$ before and after reaction (AR), Figure S5. Raman spectra and chemical maps of the Ni/ZnO before and after reaction (AR), Figure S6. Raman spectra and chemical maps of the Ni/TiSi before and after reaction (AR). Table S1: Catalyst screening in CO$_2$ methanation.

Data Availability Statement: The data presented in this study are available in Supplementary Material.

Conflicts of Interest: The authors declare no conflict of interest.

References

1. Gac, W.; Zawadzki, W.; Rotko, M.; Greluk, M.; Słowik, G.; Kolb, G. Effects of support composition on the performance of nickel catalysts in CO2 methanation reaction. *Catal. Today* **2020**, *357*, 468–482. [CrossRef]
2. Müller, K.; Fleige, M.; Rachow, F.; Schmeißer, D. Sabatier based CO2-methanation of flue gas emitted byconventional power plants. *Energy Proc.* **2013**, *40*, 240–248. [CrossRef]
3. Frontera, P.P.; Macario, A.; Ferraro, M.; Antonucci, P.L. Supported Catalysts for CO2 Methanation: A Review. *Catalysts* **2017**, *7*, 59. [CrossRef]
4. Wang, L.; Rao, M.; Diethelm, S.; Lin, T.-E.; Zhang, H.; Hagen, A.; Maréchal, F.; van Herle, J. Power-to-methane via co-electrolysis of H2O and CO2: The effects of pressurized operation and internal methanation. *Appl. Energy* **2019**, *250*, 1432–1445. [CrossRef]
5. Guerra, L.; Rossi, S.; Rodrigues, J.; Gomes, J.; Puna, J.; Santos, M.T. Methane production by a combined Sabatier reaction/water electrolysis process. *J. Environ. Chem. Eng.* **2018**, *6*, 671–676. [CrossRef]
6. He, Z.; Cui, M.; Qian, Q.; Zhang, J.; Liu, H.; Ha, B. Synthesis of liquid fuel via direct hydrogenation of CO2. *Proc. Natl. Acad. Sci. USA* **2019**, *116*, 12654–12659. [CrossRef]
7. Ashok, J.; Pati, S.; Hongmanorom, P.; Tianxi, Z.; Junmei, C.; Kawi, S. A review of recent catalyst advances in CO2 methanation processes. *Catal. Today* **2020**, *356*, 471–489. [CrossRef]
8. Zosen, H. Available online: https://www.hz-inova.com/cms/en/?p=4748 (accessed on 15 February 2021).

9. HELMETH. Available online: https://www.kit.edu/kit/english/pi_2018_009_power-to-gas-with-high-efficiency.php# (accessed on 15 February 2021).

10. Electrochaea. Available online: http://www.electrochaea.com/electrochaea-commissions-worlds-largest-power-to-gas-demonstration-project-based-on-biological-methanation/ (accessed on 15 February 2021).

11. BioCat. Available online: https://www.bio-cat.com/bio-cat-patents-microbial-enzyme-blend-for-pancreatic-insufficiency-patients/ (accessed on 15 February 2021).

12. Li, W.; Wang, H.; Jiang, X.; Zhu, J.; Liu, Z.; Guo, X.; Song, C. A short review of recent advances in CO2 hydrogenation to hydrocarbons over heterogeneous catalysts. *RSC Adv.* **2018**, *8*, 7651–7669. [CrossRef]

13. Garbarino, G.; Riani, P.; Magistri, L.; Busca, G. A study of the methanation of carbon dioxide on Ni/Al2O3 catalysts at atmospheric pressure. *Int. J. Hydrogen Energy* **2014**, *39*, 11557–11565. [CrossRef]

14. Liu, Q.; Gu, F.; Lu, X.; Liu, Y.; Li, H.; Zhong, Z.; Xu, G.; Su, F. Enhanced catalytic performances of Ni/Al2O3 catalyst via the addition of V2O3 for CO methanation. *Appl. Catal. A* **2014**, *488*, 37–47. [CrossRef]

15. Muroyama, H.; Tsuda, Y.; Asakoshi, T.; Masitah, H.; Okanishi, T.; Matsui, T.; Eguchi, K. Carbon dioxide methanation over Ni catalysts supported on variousmetal oxides. *J. Catal.* **2016**, *343*, 178–184. [CrossRef]

16. Yang, B.; He, J.; Zhang, G.; Guo, J. *Vanadium*; Elsevier: Amsterdam, The Netherlands, 2021; ISBN 978-0-12-818898-9.

17. Valentini, A.; Carreño, N.L.V.; Probst, L.F.D.; Lisboa-Filho, P.N.; Schreiner, W.H.; Leite, E.R.; Longo, E. Role of vanadium in Ni:Al2O3 catalysts for carbon dioxide reforming of methane. *Appl. Catal.* **2003**, *255*, 211–220. [CrossRef]

18. Kowalik, P.; Antoniak-Jurak, K.; Błesznowski, M.; Herrera, M.C.; Larrubia, M.A.; Alemany, L.J.; Pieta, I.S. Biofuel steam reforming catalyst for fuel cell application. *Catal. Today* **2015**, *254*, 129–134. [CrossRef]

19. SBŁ-INS Commercial Catalysts, Brochure Available on Request. Available online: http://www.ins.pulawy.pl/index.php/en/products/catalysts-and-sorbents/hydrocarbon-steam-reforming (accessed on 17 March 2021).

20. Pieta, I.S.; Pieta, P.; Nowakowski, R. Nickel-vanadium catalyst for the valorization of carbon dioxide, a method of obtaining a nickel-vanadium catalyst and the use of a nickel-vanadium catalyst in the processes of carbon dioxide hydrogenation and reforming. Polish Patent P-434122, 9 September 2020.

21. Pieta, S.I. The Method and Installation for Continuous Multi-Parameter Analysis of Gaseous Fuel Conversion Including Reforming and Measurement of Post-Reaction Gas Pollutants Nitrogen, Carbon and Sulfur Oxides and Chlorine. UP RP nr Patent P-412277, 8 May 2015.

22. Cavani, F.; Trifiro, F.; Vaccari, A. Hydrotalcite-type anionic clays: Preparation, properties and applications. *Catal. Today* **1991**, *11*, 173–301. [CrossRef]

23. di Cosimo, J.I.; Díez, V.K.; Xu, M.; Iglesia, E.; Apesteguía, C.R. Structure and surface and catalytic properties of Mg-Al basic oxides. *J. Catal.* **1998**, *178*, 499–510. [CrossRef]

24. Frost, R.L.; Palmer, S.J.; Theiss, F. Synthesis and Raman spectroscopic characterisation of hydrotalcites based on the formula Ca6Al2(CO3)(OH)16 4H2O. *J. Raman Spectrosc.* **2011**, *42*, 1163–1167. [CrossRef]

25. Kong, X.; Zheng, R.; Zhu, Y.; Ding, G.; Zhu, Y.; Li, Y.W. Rational design of Ni-based catalysts derived from hydrotalcite for selective hydrogenation of 5-hydroxymethylfurfural. *Green Chem.* **2015**, *17*, 2504–2514. [CrossRef]

26. Michalik, A.; Napruszewska, B.D.; Walczyk, A.; Krysciak-Czerwenka, J.; Duraczynska, D.; Serwicka, E.M. Synthesis of Nanocrystalline Mg-Al Hydrotalcites in the Presence of Starch-the Effect on Structure and Composition. *Materials* **2020**, *13*, 602. [CrossRef] [PubMed]

27. Napruszewska, B.D.; Michalik-Zym, A.; Dula, R.; Duraczyńska, D.; Rojek, W.; Socha, W.; Lityńska-Dobrzyńska, L.; Bahranowski, K.; Serwicka, E.M. VOCs combustion catalysts based on composites of exfoliated organo-Laponite and multimetallic (Mn, Al, Zr, Ce) hydrotalcites prepared by inverse microemulsion. *Catal. Today* **2019**, *333*, 182–189. [CrossRef]

28. Olszówka, J.E.; Karcz, R.; Michalik-Zym, A.; Napruszewska, B.D.; Bielańska, E.; Kryściak-Czerwenka, J.; Socha, R.P.; Nattich-Rak, M.; Krzan, M.; Klimek, A.; et al. Effect of grinding on the physico-chemical properties of Mg-Al hydrotalcite and its performance as a catalyst for Baeyer-Villiger oxidation of cyclohexanone. *Catal. Today* **2019**, *333*, 147–153. [CrossRef]

29. Rives, V.; Kannan, S. Layered double hydroxides with the hydrotalcite-type structurecontaining Cu2z, Ni2z and Al3z. *J. Mater. Chem.* **2000**, *10*, 489–495. [CrossRef]

30. Cheng, C.; Xu, G.; Zhang, H.; Luo, Y. Hydrothermal synthesis Ni-doped ZnO nanorods with room-temperature ferromagnetism. *Mater. Lett.* **2008**, *62*, 1617–1620. [CrossRef]

31. Zhang, K.; Mukhriza, T.; Liu, X.; Greco, P.P.; Chiremba, E. A study on CO2 and CH4conversion to synthesis gas and higherhydrocarbons by the combination of catalysts and dielectric-barrierdischarges. *Appl. Catal. A Gen.* **2015**, *502*, 138–149. [CrossRef]

32. Bantignies, J.L.; Deabate, S.; Righi, A.; Rols, S.; Hermet, P.; Sauvajol, J.L.; Henn, F. New Insight into the Vibrational Behavior of Nickel Hydroxide and Oxyhydroxide Using Inelastic Neutron Scattering, Far/Mid-Infrared and Raman Spectroscopies. *J. Phys. Chem. C* **2008**, *112*, 2193–2201. [CrossRef]

33. Feret, F.; Roy, D.; Boulanger, C. Determination of alpha and beta alumina in ceramic alumina by X-ray diffraction. *Spectrochim. Acta Part B* **2000**, *55*, 1051–1061. [CrossRef]

34. NIST. Available online: https://www.nist.gov/pml/productsservices/physical-reference-data (accessed on 15 February 2021).

35. Galvita, V.; Siddiqi, G.; Sun, P.; Bell, A.T. Ethane dehydrogenation on Pt/Mg(Al)O and PtSn/Mg(Al)O catalysts. *J. Catal.* **2010**, *271*, 209–219. [CrossRef]

36. Zhou, Q.; Chen, W.; Xu, L.; Peng, S. Hydrothermal Synthesis of Various Hierarchical ZnO Nanostructures and Their Methane Sensing Properties. *Sensors* **2013**, *13*, 6171–6182. [CrossRef] [PubMed]

37. Hu, A.; Zhang, X.; Luong, D.; Oakes, K.D.; Servos, M.R.; Liang, R.; Kurdi, S.; Peng, P.; Zhou, Y. Adsorption and Photocatalytic Degradation Kineticsof Pharmaceuticals by TiO2Nanowires During Water Treatmen. *Waste Biomass Valorization* **2012**, *3*, 443–449. [CrossRef]

38. Busca, G.; Lorenzelli, V. Infrared spectroscopic identification of species arising from reactive adsorption of carbon oxides on metal oxide surfaces. *Mater. Chem.* **1982**, *7*, 89–126. [CrossRef]

39. Gonzalez-Gil, R.; Herrera, C.; Larrubia, M.A.; Kowalik, P.; Pieta, I.S.; Alemany, L.J. Hydrogen production by steam reforming of DME over Ni-based catalysts modified with vanadium. *Int. J. Hydrogen Energy* **2016**, *41*, 19781–19788. [CrossRef]

40. Vedrine, J. Acid-base characterization of heterogeneous catalysts: An up-to-date overview. *Res. Chem. Intermed.* **2015**, *41*, 9387–9423. [CrossRef]

41. Garcia-Dieguez, M.; Pieta, I.S.; Herrera, M.C.; Larrubia, M.A.; Alemany, L.J. Improved Pt-Ni nanocatalysts for dry reforming of methane. *Appl. Catal. A Gen.* **2010**, *377*, 191–199. [CrossRef]

42. Mustapha, S.; Ndamitso, M.M.; Abdulkareem, A.S.; Tijani, J.O.; Shuaib, D.T.; Ajala, A.O.; Mohammed, A.K. Application of TiO2 and ZnO nanoparticles immobilized on clay in wastewater treatment: A review. *Appl. Water Sci.* **2020**, *10*, 49. [CrossRef]

43. Kayani, Z.N.; Naz, F.; Riaz, S.; Naseem, S. Characteristics of Al-doped ZnO:Ni films grown on glass by sol-gel dip coating technique. *J. Saudi Chem. Soc.* **2017**, *21*, 425–433. [CrossRef]

44. León, A.; Reuquen, P.; Garín, C.; Segura, R.; Vargas, P.; Zapata, P.; Orihuela, P.A. FTIR and Raman Characterization of TiO2 Nanoparticles Coated with Polyethylene Glycol as Carrier for 2-Methoxyestradiol. *Appl. Sci.* **2017**, *7*, 49. [CrossRef]

45. Amin, M.H. Relationship Between the Pore Structure of Mesoporous Silica Supports and the Activity of Nickel Nanocatalysts in the CO2 Reforming of Methane. *Catalysts* **2020**, *10*, 51. [CrossRef]

46. Hosseini, S.A.; Niaei, A.; Salari, D. Production of γ-Al2O3 from Kaolin. *Open J. Phys. Chem.* **2011**, *1*, 23–27. [CrossRef]

47. Noonuruk, R.; Techitdheera, W.; Pecharapa, W. Study of Structural Properties of NiZnO Thin Films under UV/Ozone Treatment by Atomic Force Microscopy and Fourier Transform Infrared Spectroscopy. *J. Microsc. Soc. Thail.* **2011**, *4*, 28–31.

48. Pieta, I.S.; Garcia-Dieguez, M.; Herrera, C.; Larrubia, M.A.; Alemany, L.J. In situ DRIFT–TRM study of simultaneous NOx and soot removal over Pt–Ba and Pt–K NSR catalysts. *J. Catal.* **2010**, *270*, 256–267. [CrossRef]

49. Solis, B.H.; Cui, Y.; Weng, X.; Seifert, J.; Schauermann, S.; Sauer, J.; Shaikhutdinov, S.; Freund, H.-J. Initial stages of CO2 adsorption on CaO: A combined experimental and computational study. *Phys. Chem. Chem. Phys.* **2017**, *19*, 423. [CrossRef]

50. Chernyshova, I.V.; Ponnurangam, S.; Somasundaran, P. Linking interfacial chemistry of CO2 to surface structures of hydrated metal oxide nanoparticles: Hematite. *Phys. Chem. Chem. Phys.* **2013**, *15*, 6953. [CrossRef]

51. Li, H.; Jiao, X.; Li, L.; Zhao, N.; Xiao, F.; Wei, W.; Sund, Y.; Zhang, B. Synthesis of glycerol carbonate by direct carbonylation of glycerol with CO2 over solid catalysts derived from Zn/Al/La and Zn/Al/La/M (M = Li, Mg and Zr) hydrotalcites. *Catal. Sci. Technol.* **2015**, *5*, 989–1005. [CrossRef]

52. Wang, Y.; Li, Y.; Zhou, Z.; Zu, X.; Deng, Y. Evolution of the zinc compound nanostructures in zinc acetate single-source solution. *J. Nanopart. Res.* **2011**, *13*, 5193–5202. [CrossRef]

53. Bezrodna, T.; Puchkovska, G.; Shymanovska, V.; Baran, J.; Ratajczak, H. IR-analysis of H-bonded H2O on the pure TiO2 surface. *J. Mol. Struct.* **2004**, *700*, 175–181. [CrossRef]

54. Aw, M.S.; Dražić, G.; Djinović, P.; Pintar, A. Transition metal pairs on ceria-promoted, ordered mesoporous alumina as catalysts for the CO2 reforming reaction of methane. *Catal. Sci. Technol.* **2016**, *6*, 3797–3805. [CrossRef]

55. Yuan, X.; Zhu, Z.; Tang, K.; Cheng, Y.; Xu, Z.; Yang, W. Formation and Properties of 1-D Alumina Nanostructures Prepared via a Template-free Thermal Reaction. *Procedia Eng.* **2015**, *102*, 602–609. [CrossRef]

56. Zhou, L.; Huang, J.; Yu, B.; You, T. A novel self-enhanced electrochemiluminescence immunosensor based on hollow Ru-SiO2@PEI nanoparticles for NSE analysis. *Sci. Rep.* **2016**, *6*, 1–9. [CrossRef] [PubMed]

57. Damyanova, S.; Pawelec, B.; Palcheva, R.; Karakirova, Y.; Sanchez, M.C.C.; Tyuliev, G.; Gaigneaux, E.; Fierro, J.L.G. Structure and surface properties of ceria-modified Ni-based catalysts forhydrogen production. *Appl. Catal. B Environ.* **2018**, *225*, 340–353. [CrossRef]

58. Dobrowolska, P.; Krajewska, A.; Gajda-Rączka, M.; Bartosewicz, B.; Nyga, P.; Jankiewicz, B.J. Application of Turkevich Method for Gold Nanoparticles Synthesis to Fabrication of SiO2@Au and TiO2@Au Core-Shell Nanostructures. *Materials* **2015**, *8*, 2849–2862. [CrossRef]

59. Elhalil, A.; Elmoubarki, R.; Farnane, M.; Machrouhi, A.; Sadiq, M.; Mahjoubi, F.Z.; Qourzal, S.; Barka, N. Photocatalytic degradation of caffeine as a model pharmaceutical pollutanton Mg doped ZnO-Al2O3heterostructure. *Environ. Nanotech. Monit. Manag.* **2018**, *10*, 63–72.

60. Li, W.; Liang, R.; Hu, A.; Huang, Z.; Zhou, Y.N. Generation of oxygen vacancies in visible lightactivated one-dimensional iodine TiO2photocatalysts. *RSC Adv.* **2014**, *4*, 36959. [CrossRef]

61. Jayalakshmi, G.; Saravanan, K. Surface plasmons enhanced band-edge emission in Ni nanoparticles decorated ZnO nanorods arrays architecture. *J. Lumin.* **2020**, *222*, 117049. [CrossRef]

62. Patil, S.S.; Patil, R.H.; Kale, S.B.; Tamboli, M.; Ambekar, J.D.; Gade, W.N.; Kolekar, S.S.; Kale, B.B. Nanostructured microspheres of silver @ zinc oxide:an excellent impeder of bacterial growth and biofilm. *J. Nanopart. Res.* **2014**, *16*, 2717. [CrossRef]

63. Lundegaard, L.F.; Tiruvalam, R.R.; Tyrsted, C.; Carlsson, A.; Morales-Cano, F.; Ovesena, C.V. Migrating Al species hindering NiO reduction on Alcontaining catalyst carriers. *Catal. Today* **2016**, *272*, 25–31. [CrossRef]

64. Scheffer, B.; Molhoek, P.; Moulijn, J.A. Temperature-programmed reduction of NiOsingle bondWO3/Al2O3 Hydrodesulphuriza-tion catalysts. *Appl. Catal.* **1989**, *46*, 11. [CrossRef]

65. Li, G.; Hu, L.; Hill, J.M. Comparison of reducibility and stability of alumina-supported Ni catalysts prepared by impregnation and co-precipitation. *Appl. Catal. A* **2006**, *301*, 16. [CrossRef]

66. Lemonidou, A.A.; Goula, M.A.; Vasalos, I.A. Carbon dioxide reforming of methane over 5 wt.% nickelcalcium aluminate catalysts ± effect of preparation method. *Cat. Today* **1998**, *46*, 175–183. [CrossRef]

67. Rogers, J.L.; Mangarella, M.C.; D'Amico, A.D.; Gallagher, J.R.; Dutzer, M.R.; Stavitski, E.; Miller, J.T.; Sievers, C. Differences in the Nature of Active Sites for Methane Dry Reforming and Methane Steam Reforming over Nickel Aluminate Catalysts. *ACS Catal.* **2016**, *6*, 5873–5886. [CrossRef]

68. Sahli, N.; Petit, C.; Roger, A.C.; Kiennemann, A.; Libs, S.; Bettahar, M.M. Ni catalysts from NiAl2O4 spinel for CO2 reforming of methane. *Catal. Today* **2006**, *113*, 187–193. [CrossRef]

69. Richardson, J.T.; Turk, B.; Twing, M.V. Reduction of model steam reforming catalysts: Effect of oxide additives. *Appl. Catal. A* **1996**, *148*, 97. [CrossRef]

70. Hamid, M.Y.S.; Jalil, A.A.; Rahman, A.F.A.; Abdullah, T.A.T. Enhanced reactive CO2 species formation via V2O5-promoted Ni/KCC-1 for low temperature activation of CO2 methanation. *React. Chem. Eng.* **2019**, *4*, 1126–1135. [CrossRef]

71. Chary, K.V.R.; Kishan, G.; Bhaskar, T.; Sivaraj, C. Structure and Reactivity of Vanadium Oxide Catalysts Supported on Anatase TiO2. *J. Phys. Chem. B* **1998**, *102*, 6792–6798. [CrossRef]

72. Ruitenbeek, M.; van Dillen, A.J.; deGroot, F.M.F.; Wachs, I.E.; Geus, J.W.; Koningsberger, D.C. The structure of vanadium oxide species on-alumina;anin situX-ray absorption study during catalytic oxidation. *Top Catal.* **2000**, *10*, 241–254. [CrossRef]

73. Wang, F.; He, S.; Chen, H.; Wang, B.; Zheng, L.; Wei, M.; Evans, D.G.; Duan, X. Active Site Dependent Reaction Mechanism over Ru/CeO2 Catalyst toward CO2 Methanation. *JACS* **2016**, *138*, 6298–6305. [CrossRef] [PubMed]

74. Younas, M.; Kong, L.L.; Bashir, M.J.K.; Nadeem, H.; Shehzad, A.; Sethupathi, S. Recent Advancements, Fundamental Challenges, and Opportunities in Catalytic Methanation of CO2. *Energy Fuels* **2016**, *30*, 8815–8831. [CrossRef]

75. Pan, Q.; Peng, J.; Sun, T.; Wang, S.; Wang, S. Insight into the reaction route of CO2 methanation: Promotion effect of medium basic sites. *Catal. Commun.* **2014**, *45*, 74–78. [CrossRef]

76. Pandey, D.; Deo, G. Effect of support on the catalytic activity of supported Ni−Fe catalysts for the CO2 methanation reaction. *J. Ind. Eng. Chem.* **2016**, *33*, 99–107. [CrossRef]

77. Dorner, R.W.; Hardy, D.R.; Williams, F.W.; Willauer, H.D. Heterogeneous catalytic CO2 conversion to value-added hydrocarbons. *Energy Environ. Sci.* **2010**, *3*, 884–890. [CrossRef]

78. Lu, X.; Gu, F.; Liu, Q.; Ga, J.; Liu, Y.; Li, H.; Jia, L.; Xu, G.; Zhong, Z.; Su, F. VOx promoted Ni catalysts supported on the modified bentonite for CO and CO2 methanation. *Fuel Proc. Technol.* **2015**, *135*, 34–46. [CrossRef]

79. Garcia-Dieguez, M.; Pieta, I.S.; Herrera, M.C.; Larrubia, M.A.; Alemany, L.J. Nanostructured Pt- and Ni-based catalysts for CO2-reforming of methane. *J. Catal.* **2010**, *270*, 136–145. [CrossRef]

80. Lavoie, J. Review on dry reforming of methane, a potentially more environmentally-friendly approach to the increasing natural gas exploitation. *Front. Chem.* **2014**, *2*, 81. [CrossRef]

81. Peppley, B.; Amphlett, J.; Kearns, L.; Mann, R. Methanol-steamreforming on Cu/ZnO/Al2O3catalysts. Part2. A comprehensive kinetic model. *Appl. Catal. A Gen.* **1999**, *179*, 1–2. [CrossRef]

82. Benrabbah, R.; Cavaniol, C.; Liu, H.; Ognier, S.; Cavadias, S.; Galvez, M.E.; da Costaa, P. Plasma DBD activated ceria-zirconia-promoted Ni-catalysts for plasma catalytic CO2 hydrogenation at low temperature. *Catal. Comm.* **2017**, *89*, 73–76. [CrossRef]

83. Smith, J.F.; Carlson, O.N.; Nash, P.G. The Ni-V (Nickel-Vanadium) system. *Bull. Alloy Phase Diagr.* **1982**, *3*, 342–348. [CrossRef]

84. Socrates, G. *Infrared and Raman Characteristic Group Frequencies*; Wiley: Hoboken, NJ, USA, 2001; ISBN 978-0-470-09307-8.

85. Tarte, P. Infrared spectra of inorganic alumi-nates and characteristic vibrational frequencies of AIO4 tetrahedra and A106 octahedra. *Spectrochem. Acta* **1967**, *23A*, 2127–2143. [CrossRef]

86. Lázaro, M.J.; Echegoyen, Y.; Suelves, I.; Palacios, J.M.; Moliner, R. Decomposition of methane over Ni-SiO2 and Ni-Cu-SiO2 catalysts: Effect of catalyst preparation method. *Appl. Catal. A Gen.* **2007**, *329*, 22–29. [CrossRef]

87. Xie, Y.; You, J.; Lu, L.; Wang, M.; Wang, J. Raman Spectroscopic Study of Coal Samplesduring Heating. *Appl. Sci.* **2019**, *9*, 4699. [CrossRef]